Multicolor structured illumination microscopy and quantitative control of coherent light with a digital micromirror device

Peter T. Brown[1], Rory Kruithoff[1], Gregory J. Seedorf[2], and Douglas P. Shepherd[1],✉

[1]Department of Physics and Center for Biological Physics, Arizona State University, Tempe, AZ 85287, USA
[2]Department of Pediatrics and Pediatric Heart Lung Center, University of Colorado Anschutz Medical Campus, Aurora, CO 80045, USA

Abstract

Structured illumination microscopy (SIM) is a powerful super-resolution (SR) microscopy technique which is applicable to a wide variety of biological systems because it does not impose photophysics requirements on the sample. Nevertheless, current ferroelectric or liquid crystal display spatial light modulator (SLM) based SIM instruments are expensive and slow compared with digital micromirror device (DMD) implementations, while DMD implementations either rely on incoherent projection which results in an order of magnitude lower signal-to-noise, or utilize coherent light at only a single wavelength. The primary obstacle to realizing a multicolor coherent DMD SIM microscope is the blazed grating effect due to the tilted micromirrors, and the lack of efficient quantitative approaches for dealing with such systems. To address this challenge, we develop a variety of quantitative tools which are applicable to any experiment relying on a DMD as an active diffractive element, including a closed form solution of the blaze and diffraction conditions, a forward model of DMD diffraction, and a forward model of coherent pattern projection. We demonstrate their power by using periodic patterns to directly map the optical transfer function of our microscope, an approach that was previously computationally infeasible. Finally, we apply these techniques to SIM by identifying experimentally feasible configuration for combinations of three and four common fluorophore wavelengths. Based on these advances, we constructed a custom DMD SIM microscope using three wavelengths and coherent light and validated this instrument by demonstrating resolution enhancement for known calibration samples, fixed cells, and live cells. This low-cost setup opens the door to applying SIM more broadly in live cell and other time-resolved experiments.

Correspondence: *douglas.shepherd @asu.edu*

The development of wavefront control using spatial light modulators (SLM's) has enabled a variety of techniques relevant to the study of biological and atomic systems, including quantitative phase imaging (1, 2), optical trapping (3–5), adaptive optics (6), production of arbitrary optical potentials, and quantum gas microscopy (7). SLM's are highly reconfigurable, which allows experiments to be modular and take advantage of dynamic light patterns. They are also highly reproducible and offer microscopic control of wavefronts, which allows precise calibration of optical systems and enhances quantitative modeling of experiments. Due to this broad applicability, advancements in optical methodology for SLM's have had an immediate impact for many fields of quantitative imaging.

The study of biological regulation at the molecular level is one field that has greatly benefited from advancements in optical methodologies. For example, the development of super-resolution (SR) microscopy has allowed optical study of biological systems below the diffraction limit, on the $1 \, \text{nm}$–$200 \, \text{nm}$ scale. Despite the promise of sub-diffraction studies of molecular interactions, SR techniques have yielded limited insight into the dynamics of molecular regulation within living cells and larger systems. One barrier is that all SR methods impose a trade-off between imaging speed, resolution, sample preparation, and fluorophore photophysics. For example, single molecule localization microscopy (SMLM) trades temporal resolution for spatial resolution, requiring fixed samples and repeated imaging of fluorophores with specific photophysics (8, 9). Computational methods that infer SR information from fluctuating signals relax the above requirements, but require acquisition, processing, and merging of many imaging frames (10, 11). Stimulated emission depletion (STED) requires a high intensity depletion beam, careful alignment of the depletion and excitation beams, specific fluorophores, and raster scans to build an image (12, 13). MINFLUX lowers the total intensity incident on the sample as compared to STED, but still requires raster scanning (14). Methods such as MoNaLISA parallelize the application of depletion and saturation to imaging, but require precise 3D pattern pro-

jection and specific fluorophore photophysics (15, 16). In contrast, structured illumination microscopy (SIM) does not impose specific sample requirements. The trade-off for this flexibility is a modest increase in high frequency content for linear SIM, requirement for high quality control of the excitation light, and potentially slow imaging rates.

SIM obtains SR information by projecting a sinusoidal illumination pattern on the sample and relying on the Moiré effect to down-mix high-frequency sample information below the diffraction limit. It was first proposed as an SR technique in (17, 18), but a similar technique was previously exploited for optical sectioning (OS) (19, 20). Early implementations achieved SR in the lateral direction only (2D-SIM) (21, 22), while later approaches also enhanced the axial resolution (3D-SIM) (23–26). Initial experiments utilized diffraction gratings to produce SIM patterns and required both separate paths for multiple colors and physical translation and rotation, which severely limited their speed (25). Various advances in LCD and ferroelectric SLM's, sCMOS cameras, and GPU's have enabled much faster 2D (27–32) and 3D SIM (33), and multicolor SIM with a single optical path (34). Recent experiments have extended SIM techniques to localization microscopy (35). The quality of the obtained SIM reconstructions is highly dependent on the modulation depth of the projected patterns and any other deviations from the ideal optical transfer function used to weight the different frequency components. As the complexity of the desired result increases from obtaining optical sectioning to multicolor 3D-SIM, so does the required required fidelity in the final projected high quality patterns. This has led to wide spread adoption of ferroelectric SLM's for high-speed SIM, despite their drawbacks which include cost, relatively slow speed, and low diffraction efficiency.

Digital micromirror devices (DMD's) are a promising alternative to ferroelectric and LCD SLM's for a variety of wavefront shaping tasks. DMD's offer several advantages, including a potential factor of 5–10 imaging rate increase, less experimental timing complexity, a factor of 2–10 lower cost, and enhanced diffraction efficiency (36–38). DMD's can reach frame rates of up to $30\,\text{kHz}$, exceeding the rate achievable in ferroelectric and liquid crystal SLM's by a factor of ~5 and ~10 respectively. Unlike ferroelectric SLM's, DMD's do not require the pattern to be inverted every $\sim100\,\text{ms}$. Finally, the amplitude-only modulation characteristic of the DMD allows fast, well-defined diversion of the illumination beam from the sample, making an additional fast shutter unnecessary. However, DMD use is currently limited by a computationally expensive forward model (37) to evaluate the blazed grating effect, which enhances the diffraction efficiency into a single order but also imposes severe restrictions on multicolor operation. To date, DMD-SIM approaches have used incoherent projection (39) or one coherent wavelength (37, 38, 40). Incoherent projection SIM at best provides an order of magnitude lower signal-to-noise ratio, leading to inferior experimental resolution, despite previously reported erroneous resolution measurements (39, 41) (Supplemental Note 9.3).

Here, we overcome these difficulties to realize three wavelength, 2D linear SIM using coherent light and a DMD. We achieve this by creating analytic forward models of light diffraction off of a DMD and pattern projection to the sample plane. We use these models to design an optical configuration that satisfies the unique requirements that a DMD imposes when used as a diffractive optic for multiple wavelengths. This framework allows us to create a calibration routine to directly map the optical transfer function (OTF) of the system without the need to estimate it from sub-diffraction limited fluorescent microspheres. We provide simulations and experimental verification of this framework for calibration and fixed samples.

1: Principles of multicolor DMD SIM using coherent light

Leveraging the advantages of the DMD in a multicolor setting requires a tractable forward model of DMD operation. To this end, we provide an analytic solution of the combined blaze and diffraction condition for arbitrary incidence angles and derive an analytical forward models of DMD diffraction and pattern projection. This provides an alternative framework to a previously published numerical simulation approach (37). We use our approach to perform detailed calculations of DMD diffraction of SIM patterns and apply these to directly measure the OTF and realize multicolor coherent SIM.

1.1. DMD diffraction forward model. To develop the DMD forward model, we calculate the diffracted light profile for an incident plane wave in the Fraunhofer approximation by considering the phase shift introduced by each point on the micromirror surfaces (37, 42–44). We adopt the same coordinate system as (37), where the DMD normal is along the $-\hat{\mathbf{z}}$ direction, the micromirrors are organized in a regular grid aligned with the $\hat{\mathbf{x}}$ and $\hat{\mathbf{y}}$ directions, and the micromirrors swivel about an axis along the $\mathbf{x} \hat{+} \mathbf{y}$ direction. For a plane wave of wave vector $k = 2\pi/\lambda$ incident along direction $\hat{\mathbf{a}}$,
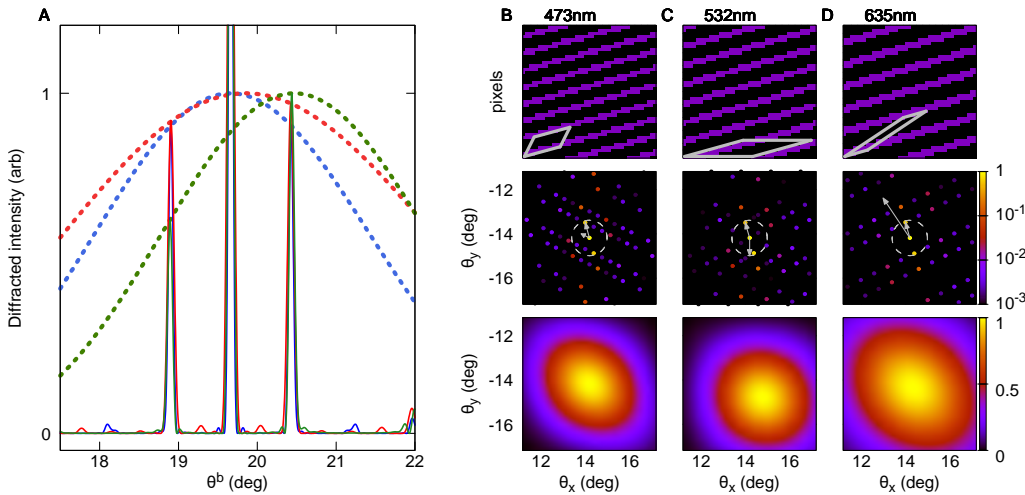
Fig. 1. A. Diffracted intensity for $\theta^a = 43.66°$ and $\lambda = 473\,\mathrm{nm}$ (blue), $\theta^a = -3.53°$ and $532\,\mathrm{nm}$ (green), and $\theta^a = 43.86°$ and $635\,\mathrm{nm}$ (red). For these input angles, $473\,\mathrm{nm}$ satisfies the Blaze condition, and $635\,\mathrm{nm}$ satisfies it to within a fraction of a degree. $532\,\mathrm{nm}$ shows a larger deviation, visible in the shift of the envelope center and the asymmetry in the diffraction peaks. To ensure the diffraction peaks for all colors appear at the same location and along the $\theta_x = -\theta_y$ line the patterns simulated here have periods of 5, 5.62, and 6.71 mirrors which are not commensurate with the pixel lattice. **B**. DMD mirror pattern showing "on" mirrors (purple), "off" mirrors (black), and one unit cell (gray outline) for $\mathbf{r}_1 = (11, 3)$ and $\mathbf{r}_2 = (3, 6)$ (upper panel). Diffracted intensity from the DMD using $473\,\mathrm{nm}$ light incident at $\theta_{x-y} = 43.66°$ shown on a log scale. The maximum acceptance angle (gray circle) and reciprocal vectors (gray arrows) are shown (center panel). The envelope function illustrating where the blaze condition is satisfied, shown with a linear scale. **C**. panels the same as B, but for $532\,\mathrm{nm}$ light incident at $-3.53°$ with $\mathbf{r}_1 = (18, 5)$ and $\mathbf{r}_2 = (21, 0)$. **D**. $635\,\mathrm{nm}$ light incident at $43.86°$ with $\mathbf{r}_1 = (7, 2)$ and $\mathbf{r}_2 = (18, 12)$.

the diffracted electric field in direction $\hat{\mathbf{b}}$ is

$$E(\hat{\mathbf{b}}) = E_o \sum_{m_x, m_y} \exp\left(-ikd(m_x, m_y) \cdot (\hat{\mathbf{b}} - \hat{\mathbf{a}})\right)$$

$$\times \quad w^2 \mathrm{sinc}\left(\frac{kw}{2} A_+(\gamma_{m_x, m_y})\right) \mathrm{sinc}\left(\frac{kw}{2} A_-(\gamma_{m_x, m_y})\right) \tag{1}$$

$$A_\pm(\gamma, \hat{\mathbf{a}} - \hat{\mathbf{b}}) = \frac{1 \pm \cos\gamma}{2}(a_x - b_x) + \frac{1 \mp \cos\gamma}{2}(a_y - b_y) \mp \frac{\sin\gamma}{\sqrt{2}}(a_z - b_z), \tag{2}$$

where γ_{m_x, m_y} is the angle the mirror at position (m_x, m_y) makes with grating normal, w is the mirror width, and d is the spacing between adjacent mirrors. At each mirror γ takes one of two values: either $12°$ ("on") or $-12°$ ("off"). Here the sinc envelope expresses the effect of rays interfering from the same micromirror, and the sum represents rays interfering from different micromirrors.

To incorporate DMD diffraction into the overall optical system response, we recast the effect of the DMD as an effective pupil function. To do this we define the pattern function, $P(m_x, m_y)$ where we take $P = 0$ ($P = 1$) at "off" ("on") mirrors. We recognize that eq. 2 gives the discrete Fourier transform (DFT) of the pattern function, $\tilde{P}$, therefore the diffracted electric field becomes

$$E(\mathbf{f}) = \tilde{P}(\mathbf{f}) H_{\mathrm{DMD}}(\mathbf{f}) \tag{3}$$

$$H_{\mathrm{DMD}}(\mathbf{f}) = w^2 \mathrm{sinc}\left[A_+\left(\gamma, \hat{\mathbf{a}} - \hat{\mathbf{b}}(\mathbf{f})\right)\right] \mathrm{sinc}\left[A_-\left(\gamma, \hat{\mathbf{a}} - \hat{\mathbf{b}}(\mathbf{f})\right)\right] \tag{4}$$

where $\mathbf{f}$ is the spatial frequency of the DMD image, $\mathbf{b}_o$ is the vector satisfying the diffraction condition, and $\hat{\mathbf{b}}(\mathbf{f})$ is the output unit vector diffracted by the pattern component at $\mathbf{f}$. We ignore the "off"-state mirrors in this equation, as we are only considering frequencies near a single solution of the diffraction condition, and the sinc envelopes for the "on" and "off" state mirrors are typically well separated.

The complete information about the pattern is contained in a discrete set of output angles (frequencies) given by the DFT frequencies

$$\frac{b_{x,y}(\mathbf{f}) - a_{x,y}}{\lambda} = \frac{1}{d}\left(\frac{n_x}{N_x}, \frac{n_y}{N_y}\right), \quad n_x, n_y \in \mathbb{Z}. \tag{5}$$

When n_x (n_y) is a multiple of N_x (N_y) eq. 5 is the diffraction condition for the underlying grating. Other frequencies are generated by diffraction from the DMD pattern. For a finite pixel grid,

intermediate frequencies can be calculated from the DFT using an analog of the Whittaker-Shannon interpolation formula.

Equations 3–5 constitute a complete forward model of DMD diffraction. The expressions obtained here remove the need to numerically evaluate integrals or perform other expensive numerical simulations to determine DMD diffraction. It is only necessary to calculate a discrete Fourier transform, solve for output angles, and evaluate the sinc factor.

wavelength	θ^a_{x-y}	diffraction order	η^2	m
473 nm	43.66°	(4, 4)	1	1
532 nm	−3.53°	(-4, -4)	0.95	0.9997
635 nm	43.86°	(3, 3)	0.66	0.979

Table 1. Comparison of modulation contrast degradation in SIM patterns due to violation of the blaze condition versus wavelength for the 5 mirror period patterns shown in Fig. 1.

1.2. Multicolor DMD diffraction. We now apply our forward model to evaluate the constraints it places on multicolor operation. We first specialize to the plane in which the micromirrors swivel, i.e. the $(x - y)\, z$ plane, which simplifies the analysis because light incident in this plane has its primary diffraction orders in the same plane. For light incoming and outgoing in this plane, the blaze and diffraction conditions reduce to (42),

$$\theta^a - \theta^b \;=\; 2\gamma \tag{6}$$

$$\sin\theta^a - \sin\theta^b \;=\; \sqrt{2}\frac{\lambda_i}{d}n_i, \tag{7}$$

where $\theta^{a,b}$ be the angles between $\hat{\mathbf{a}}$ or $\hat{\mathbf{b}}$ and the DMD normal in the $(x - y)\, z$ plane and i indexes the different wavelengths. The blaze condition (eq. 6) is the angle where the law of reflection is satisfied for light incident on a single micromirror (42). For N wavelengths, this is a system of $N + 1$ equations with two angles and N diffraction orders as free parameters. In Supplemental Note 1 we show the blaze and diffraction conditions can be solved analytical for arbitrary input angles.

To realize multicolor operation we must solve this system for $N > 1$, which we achieve by first solving the blaze and diffraction conditions for λ_1, and then attempting to satisfy $\frac{\lambda_i}{\lambda_j} = \frac{n_j}{n_i}$. This ratio condition can be solved by finding rational approximations to each of these, $\frac{\lambda_i}{\lambda_1} = \frac{p_i}{q_i}$. Then an approximate solution is obtained from $n_1 = \mathrm{lcm}(p_1, ..., p_n)$ and $n_i = \frac{q_i n_1}{p_i}$. Any deviation between the rational approximation and the wavelength ratio must be accounted for by changing the input angle of the incident light, which entails slight violations of the blaze condition.

Additional colors can also be injected using the DMD mirror state "off" state. Supposing we have already fixed the input and output angle for several colors using the "on" state mirrors, the condition additional wavelengths must satisfy is

$$\sin(\theta^a - 4\gamma) - \sin(\theta^a - 2\gamma) = \sqrt{2}\frac{\lambda}{d}n. \tag{8}$$

For our DMD parameters, $d = 7.56\,\mu\mathrm{m}$ and $\gamma = 12°$, two color operation can be achieved using $\lambda_1 = 473\,\mathrm{nm}, \lambda_2 = 635\,\mathrm{nm}$, by approximating $\lambda_2/\lambda_1 \sim 4/3$ which implies $n_1 = 4, n_2 = 3$, with $\theta^a \sim 43°$ and $\theta^b \sim 19°$. Adding a third wavelength, $\lambda_3 = 532\,\mathrm{nm}$, using this approach is challenging because the smallest rational approximation with less than $10\,\%$ error is $\lambda_3/\lambda_1 \sim 8/7$, implying $n_1 = 8, n_2 = 7, n_3 = 6$. However, the maximum diffraction orders allowed by eqs. 6 and 7 are $n_{\max} = 4, 3, 3$ respectively. Instead, we achieve three color operation by injecting $532\,\mathrm{nm}$ light using $\theta^a = -3.5°$ and the -4 order from the "off" mirrors. Overlapping the $532\,\mathrm{nm}$ diffraction with the other colors requires a deviation of $\sim 1.5°$ from the blaze condition. Perfect alignment of the -4th order occurs near $550\,\mathrm{nm}$.

Deviations from the blaze condition degrade the SIM modulation contrast. To quantify this degradation, let η be the imbalance between the two components of the diffracted electric field that interfere to produce the SIM pattern. The pattern modulation contrast is the ratio of amplitudes of the high frequency and DC components,

$$m \;=\; \frac{2\eta}{1 + \eta^2}. \tag{9}$$

The contrast depends on the angle of the SIM pattern, ranging from a minimum along the $\theta_x = -\theta_y$ direction to a maximum along the $\theta_x = \theta_y$ direction. We summarize the worst case contrast for our parameters in table 1 and fig. 1, where we find high contrast is expected despite the modest violation of the blaze condition at $532\,\mathrm{nm}$.

1.3. DMD SIM forward model. To quantitatively characterize SIM pattern formation in our system, we apply the DMD forward model to a set of mirror patterns commonly employed to generate SIM sinusoidal illumination profiles. SIM patterns are designed to be periodic to maximize diffraction into a single spatial frequency component. We define SIM patterns on a small subset of DMD mirrors, the unit cell, which is tiled across the DMD by a pair of lattice vectors, $\mathbf{r}_1$ and $\mathbf{r}_2$, which have integer components. This produces a periodic pattern in the sense that mirrors separated by $n\mathbf{r}_1 + m\mathbf{r}_2$ for any $n, m \in \mathbb{Z}$ will be in the same state.

The lattice structure implies all frequency components of the SIM pattern are multiples of the reciprocal lattice vectors, $\mathbf{k}_{1,2}$, defined by the property $\mathbf{r}_i \cdot \mathbf{k}_j = \delta_{ij}$ (45). This constrains the frequencies of the diffracted electric field to the set $\mathbf{f} = n_1 \mathbf{k}_1 + n_2 \mathbf{k}_2$. Furthermore, the Fourier components can be calculated from the unit cell U, which is typically much smaller than the full DMD,

$$\tilde{P}(s,t) \quad = \quad \sum_{(i,j) \in U} P(i,j) \exp\left[-2\pi i(i,j) \cdot (s\mathbf{k}_1 + t\mathbf{k}_2)\right]. \tag{10}$$

This expression is correct up to a boundary term when the unit cell does not perfectly tile the DMD.

To generate appropriate SIM patterns for the experiment we construct $\mathbf{r}_{1,2}$ such that $\mathbf{k}_2$ matches a desired period P and angle θ (see Supplemental Note 6). We also require that the pattern can be translated to change its phase, which is achieved by setting $\mathbf{r}_2 = (n,m)n_p$ where n_p is the number of desired SIM phases (29, 30, 33, 34). Next, we construct one unit cell of our pattern by generating a smaller cell U_p from the vectors $\mathbf{r}_1$ and $\mathbf{r}_2/n_p$. By construction U_p is contained in U. Setting all pixels in U_p to "on" and all other pixels in U to "off" creates the desired pattern, which has Fourier components

$$\tilde{P}(s,t) \quad = \quad \sum_{(i,j) \in U_p} \exp\left[-2\pi i(i,j) \cdot (s\mathbf{k}_1 + t\mathbf{k}_2)\right]. \tag{11}$$

The strongest Fourier component of this pattern occurs at $\mathbf{k}_2$, which defines the SIM frequency. However the pattern also has Fourier weight at other reciprocal lattice vectors due to its binary and pixelated nature. These parasitic Fourier components introduce unwanted structure in the SIM patterns, and are blocked in the experiment by inserting a mask in the Fourier plane.

1.4. Optical transfer function determination. SIM reconstruction relies on detailed knowledge of the optical transfer function, which is typically only known theoretically or inferred from the point-spread function with low resolution. We utilize our DMD and SIM pattern forward models to directly measure the optical transfer function by projecting a sequence of SIM patterns, including parasitic diffraction orders, on a fluorescent sample and comparing the strength of different Fourier components with our model predictions. Such an approach may also be useful for higher resolution pupil phase retrieval schemes (46).

To map the optical transfer function, we project a series of SIM patterns with different frequencies and angles on a sample slide containing a thin layer of dye and observe the fluorescence at the camera. To avoid additional complications, we remove all polarization optics along the DMD path. For each pattern, we extract the amplitudes of the Fourier peaks at many reciprocal lattice vectors. We normalize the peak heights by the DC pattern component to correct for laser intensity drift. Finally, we compare the result to the Fourier components of the intensity pattern, as predicted by our forward model. The ratio of the measured and predicted peak value gives the optical transfer function of the imaging system. The results of this measurement are shown in Fig. 2.

The optical transfer function can be estimated from

$$H(\mathbf{f}_i) \quad = \quad \frac{I(\mathbf{f}_i)}{m(\mathbf{f}_i)e^{i\phi(\mathbf{f}_i)}}, \tag{12}$$

where I is the Fourier transform of the camera image, H is the optical transfer function, the $\mathbf{f}_i$ are the allowed Fourier components of the DMD pattern, and the m and ϕ are the amplitude and phase of intensity pattern generated by the DMD (Supplemental Note 3).
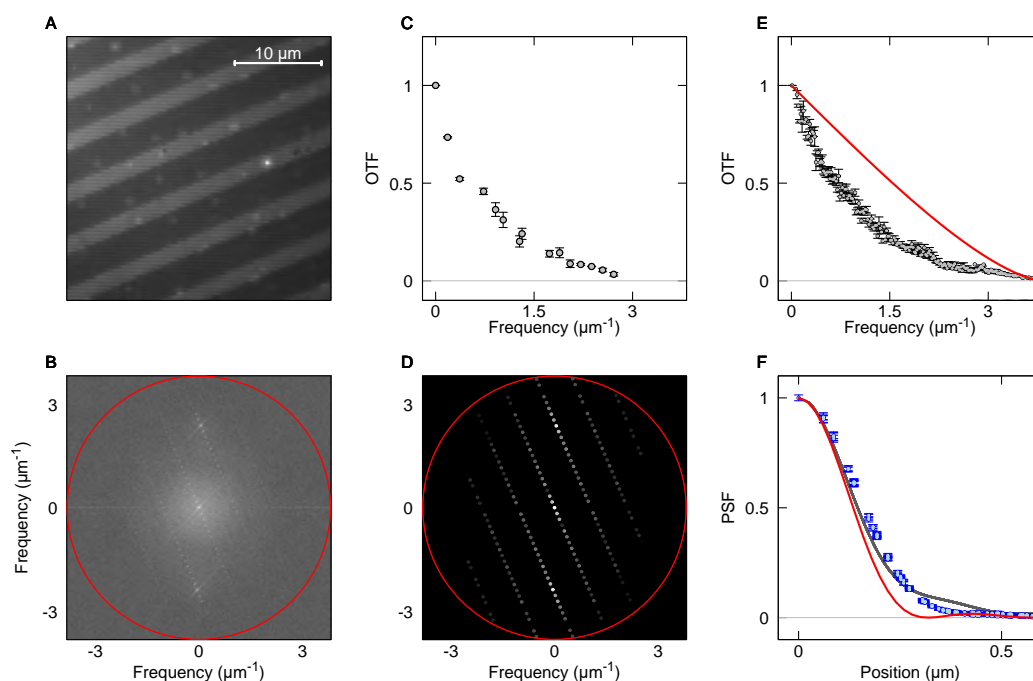
Fig. 2. Experimental optical transfer function determination. A. Image of Alexa Fluor 647 dye slide excited with $473\,\text{nm}$ light and a DMD pattern with lattice vectors $\mathbf{r}_1 = (-107, -106)$ and $\mathbf{r}_2 = (111, 117)$. **B.** Power spectrum of image from A. illustrating the discrete set of pattern diffraction frequencies. The red line denotes the maximum frequency passed by the imaging system. **C.** Peak heights obtained from the Fourier transform of A. divided by the expected intensity components of the DMD pattern. Only peaks that are expected to be larger than $1\,\%$ of the DC value are shown. These provide an experimental estimate of the optical transfer function (gray points). Error bars are estimated from the noise power beyond the band cutoff. **D.** Theoretical power spectrum of the intensity pattern. The set of discrete frequency components predicted by the forward model matches that seen in the experiment. **E.** Experimental OTF (gray) determined with ~ 3800 peaks from 360 patterns as in C. These points are binned and the error bars represent the standard error of the mean. The red line is the theoretical optical transfer function for a circular aperture and $\text{na} = 1.3$. **F.** Point spread functions corresponding to the OTF's shown in E., including the ideal PSF for a circular aperture (red), the PSF obtained from the OTF (gray), and the PSF obtained from imaging diffraction limited beads (blue).

The experimental OTF rolls of more sharply than the ideal, which is expected for real optical systems. The point spread function obtained from the OTF agrees well with that obtained from diffraction limited beads (Fig. 2F). We use this experimental OTF in the reconstruction of our SIM data, which is expected to lead to more accurate reconstructions (Supplemental Note 9).

This approach can also be applied in real samples if additional corrections for sample structure are included. Incorporating this quantitative OTF measurement technique with adaptive optics would allow sensorless real-time aberration correction similar to what was achieved in (47), but incorporating additional information from our quantitative model.

2: Experimental results

We designed a DMD SIM microscope for three-color coherent light operation based on the theoretical approach described above. With this instrument, we realize three-color imaging at $470\,\text{nm}$ or $473\,\text{nm}$, $532\,\text{nm}$, and $635\,\text{nm}$ over a $90\,\mu\text{m} \times 90\,\mu\text{m}$ field of view using a $100\times$ fluorite objective with $\text{na} = 1.3$. Details of the optical path are given in Supplemental Note 4.

We validated this instrument's capabilities by performing SIM on a variety of samples, including an Argo-SIM calibration sample which shows our instrument produces SR information in all spatial directions and achieves resolution near the theoretical limit, and measurements of fixed and live cells which demonstrate two- and three-color imaging with SR enhancement in biological systems. Sample preparation is described in Supplemental Notes 5.

To support our instrument, we created a Python-based software suite for forward models of DMD diffraction and pattern projection, DMD pattern design, OTF measurement analysis, simulation of SIM imaging given a ground truth structure, and 2D SIM reconstruction. We bench marked our approach using a variety of simulations (Supplemental Note 9) as well as compared to FairSIM (Supplemental Note 8). Our approach is built on previously published works, with enhancements based on our

ability to precisely calibrate fringe projection and direct measurement of the OTF. All analysis code is available on GitHub `https://github.com/QI2lab/mcSIM`.

2.1. Estimating SIM resolution from variably spaced line pairs. We assessed the experimental SIM resolution by measuring the Argo-SIM test slide (Fig. 3). This slide includes test patterns consisting of variably spaced lines, ranging from 390 nm to 0 nm in steps of 30 nm. There are four of these patterns in different orientations (0°, 45°, 90°, 135°), allowing determination of the SIM resolution in all directions (Fig. 3A). We only assessed performance in the 473 nm channel because the other channels do not efficiently excite fluorescence in the sample.

The smallest line pair we resolved is separated by 120 nm (10th pair, Fig. 3E). This should be compared with the minimum line spacing resolved by the widefield image, which is the 270 nm spaced pair (5th). The upper theoretical bound on SIM resolution is set by the pattern spacing. The maximum theoretical resolution for $\lambda \sim 520$ nm, na = 1.3, and SIM pattern period 250 nm–260 nm is $\sim$110 nm, which is within experimental uncertainty of the measured resolution.

This same performance is theoretically achievable in biological samples although in practice the resolution is often limited by maximum signal-to-noise ratio, which is determined by available laser power, fluorophore brightness, and sample aberrations. The highest frequency SR information falls at the edge of the OTF, and the intensity must exceed the background noise to be detectable. We further explored the role of signal-to-noise ratio and the use of our calibrated OTF via simulations (Supplemental Note 9).
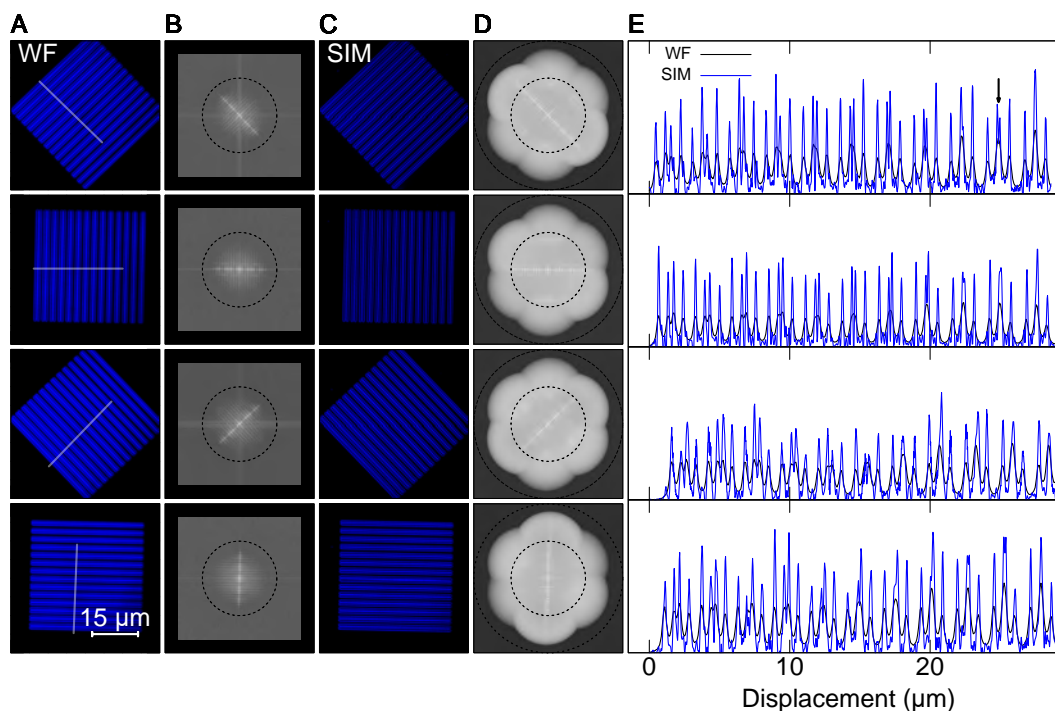

Fig. 3. Experimental characterization of SIM resolution. A. Widefield images for 473 nm excitation light and different pattern orientations shown in analog-to-digital units (ADU). **B**. Power spectra of the images from A. The black circle illustrates the maximum frequency where the ideal optical transfer function has support for na = 1.3 and emission wavelength 519 nm. For comparison with the SIM power spectrum, the widefield power spectrum is shown on the same frequency axes. Due to the sampling rate, the widefield image does not contain the highest frequencies present in the SIM image. We display a black background for these higher frequencies. **C**. SR-SIM images. **D**. Power spectra of SR-SIM images from D. The smaller circle as in B. The larger circle has twice the diameter, representing the maximum theoretical resolution for (linear) SIM. **E**. One-dimensional cuts plotted along the lines illustrated in A., showing 11 line pairs with spacings ranging from 390 nm to 90 nm in 30 nm steps. We show the widefield image (black) and SR-SIM image (blue). The 5th line pair, with spacing 270 nm, is the closest spaced pair visible in the widefield. The arrow in the top panel identifies 10th line pair, with spacing 120 nm, which is the closest spaced line pair we distinguish in the SR-SIM reconstructions.

2.2. Two-wavelength imaging of fixed cells. As an initial test of multicolor imaging using both "on" and "off" states of the DMD, we performed two wavelength SIM using the 473 nm and 532 nm channels to image actin filaments and mitochondria labeled with Alexa Fluor 488 and MitoTracker Red CMXRos in fixed bovine pulmonary artery endothelial (BPAE) cells. The SIM images substantially narrow the apparent width of the actin filaments (Fig. 4), in many cases making two filaments

visible that were not distinguishable in the widefield image. The mitochondria similarly reveal cristae which cannot be distinguished in the widefield, but are clearly visible in the SIM. We verified our reconstruction results using FairSIM (Supplemental Figure 4) and further explored signal-to-noise in filamentous networks via simulation (Supplemental Note 9).

We assess the SIM resolution enhancement using a parameter-free decorrelation analysis technique (48), which is available as an ImageJ plugin. Decorrelation analysis, which infers the resolution based on phase correlations in Fourier transform of the image, is expected to provide an accurate resolution estimate for sCMOS data, while Fourier ring correlation is not (49–51). For a conservative estimate of resolution enhancement, we use decorrelation analysis to estimate the relative resolution enhancement between the deconvolved and SIM images. For the BPAE cell sample, we find SIM leads to resolution enhancements by factors of ~ 1.5 and ~ 1.65 in the $473\,\text{nm}$ and $532\,\text{nm}$ channels respectively.
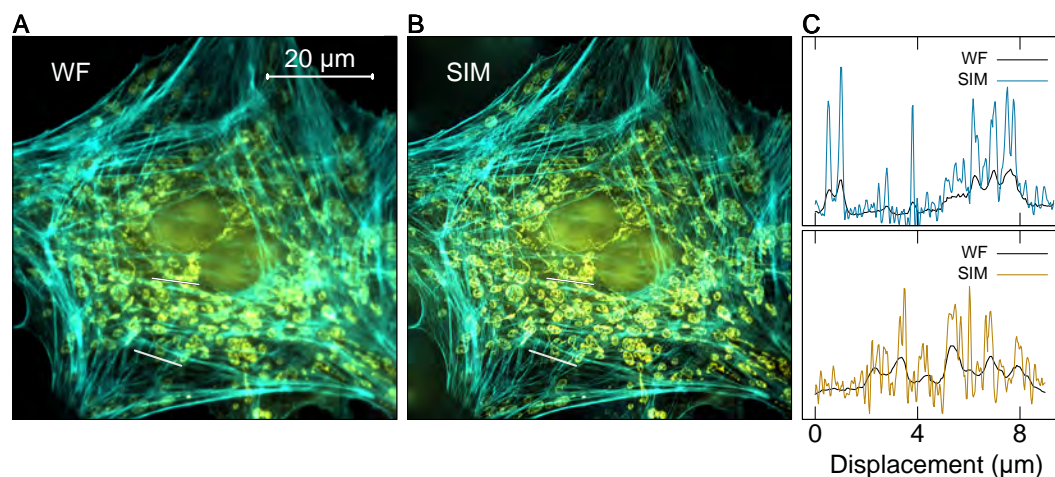

Fig. 4. Two-color imaging of BPAE cells A. Widefield image of a BPAE cell showing actin filaments in the $473\,\text{nm}$ channel (cyan), and mitochondria in the $532\,\text{nm}$ channel (yellow). Images are displayed in ADU. **B.** SIM-SR reconstruction corresponding to the image in A. **C.** One-dimensional cuts plotted along the lines illustrated in A. and B. We show the widefield image (black line) and SR-SIM image (colored line) for the $473\,\text{nm}$ excitation (top) corresponding to the lower line in A. and $532\,\text{nm}$ excitation (bottom) corresponding to the upper line in A. The SIM traces show significant enhancement of resolution and features which cannot be distinguished in the widefield image.

2.3. Three-wavelength imaging of live adenocarcinoma epithelial cells. We demonstrated time-resolved three-color SIM of live human adenocarcinoma cells to image mitochondria, actin, and lysosomes labeled with MitoTracker green, CellMask orange, and LysoTracker deep red. We imaged cell dynamics over a period of $15\,\text{min}$ with a field of view of $90\,\mu\text{m} \times 90\,\mu\text{m}$, taking images at $1\,\text{min}$ intervals (see Supplemental Movies 1 and 2). We chose an exposure time of $50\,\text{ms}$ for raw SIM images, corresponding to $0.45\,\text{s}$ per color and $1.65\,\text{s}$ for a full three-color image. We chose the longest acquisition time such that mitochondria and lysosome dynamics were negligible during the 9 SIM images, which maximizes the SIM SNR. Our setup can realize single frame exposure times down to $\sim 3\,\text{ms}$, limited by the speed of the TriggerScope. Using a fast DAQ could allow us to reach the minimum exposure time allowed by the DMD, $\sim 0.1\,\text{ms}$. However, in most experiments sample properties such as SNR and fluorophore brightness provide a practical speed limit.

A single frame is shown in fig. 5, demonstrating enhanced contrast in the SIM image for the mitochondria and lysosomes and reveals branching of actin filaments which cannot be resolved in the widefield. Applying decorrelation analysis reveals resolution enhancement of 1.3, 1.65, and 1.4 in the $470\,\text{nm}$, $532\,\text{nm}$, and $635\,\text{nm}$ channels respectively.
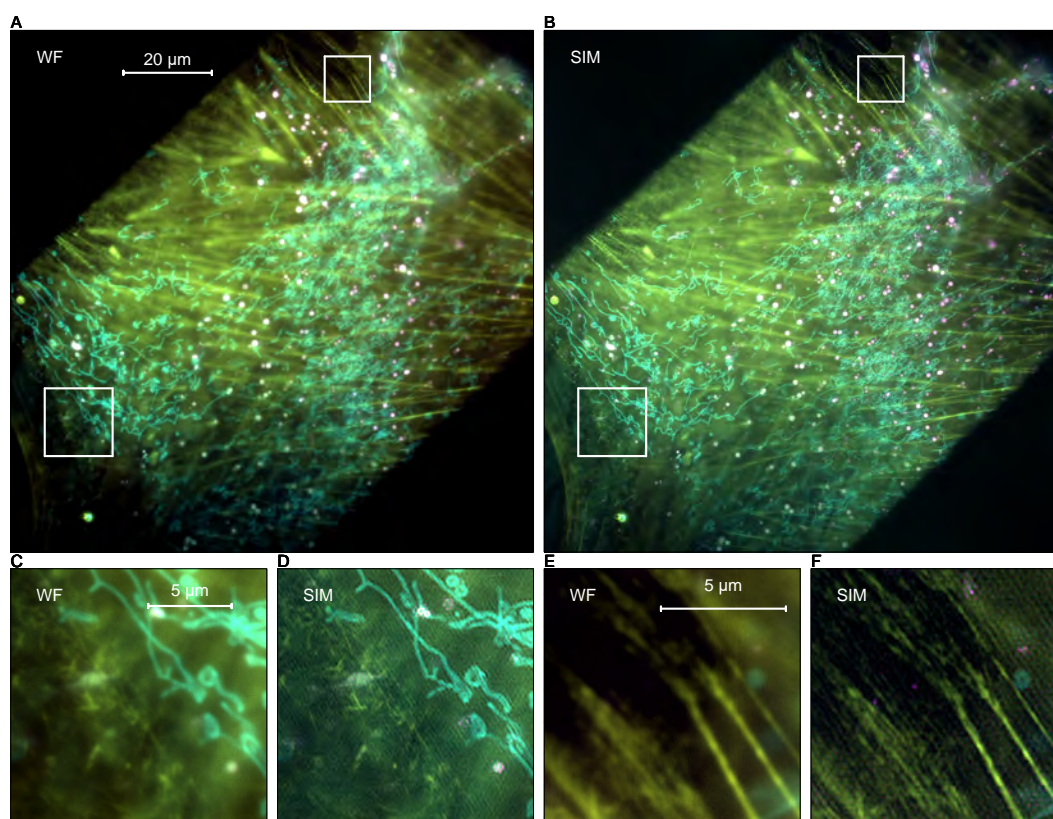
Fig. 5. Three-color imaging of live human adenocarcinoma epithelial cells A. Widefield image of human adenocarcinoma epithelial cell showing actin filaments (yellow) in the $532\,\text{nm}$ channel, lysosomes (purple) in the $635\,\text{nm}$ channel, and mitochondria (cyan) in the $470\,\text{nm}$ channel. The field of view is limited by the size of the DMD, which is visible as the bright rectangular region in the image. Images are displayed in ADU. **B**. SIM-SR reconstruction corresponding to the image in A. **C, D**, Widefield and SIM images of the lower-left region of interest illustrating resolution enhancement for the mitochondria and actin filaments. Various short actin filaments that are difficult to see in the widefield image are visible in the SIM image with higher contrast, and their width is considerably narrowed. **E, F**,. Widefield and SIM images of a the upper-right region of interest illustrating resolution enhancement for several longer actin filaments.

3: Discussion

Multi-wavelength coherent SIM is regularly achieved using diffraction gratings or SLM's for fringe projection, but the maximum achievable pattern display rate is limited by physical translation and rotation of the grating or the refresh rate of the SLM. Here, we provide a new theoretical framework to leverage a DMD as the diffractive optic for multi-wavelength coherent SIM, extending previous work (37, 38). Our work significantly differs from previous SIM approaches using multi-wavelength incoherent LED light sources or multi-wavelength incoherent image projection using a DMD (39, 52). In the current work, the maximum resolution is governed by the coherent transfer function and does not require hundreds to thousands of raw images to generate a SIM image, or require scanning.

This opens the possibility for quantitative, multi-wavelength pattern formation at rates up to $30\,\text{kHz}$ for a factor of ~5 lower cost than SLM based units. While SIM imaging rates are ultimately limited by signal-to-noise ratio and phototoxicity, fast control of multi-wavelength pattern formation also provides new avenues in the design of multi-wavelength tomography (1, 2), multi-wavelength optical trapping (3–5, 7), high-speed tracking of photostable fluorescent labels below the diffraction limit (53), and high-speed modulation enhanced localization microscopy in multiple colors (35, 40, 54).

Future improvements to our approach may include extension to more wavelengths (see Supplemental Note 1), 3D-SIM (33, 34), online GPU processing to speed reconstruction (32), specialized pattern generation to account for rolling shutters (55), and multiple cameras to speed multi-wavelength acquisition. Ease of alignment and instrument flexibility could be improved by removing the need for the Fourier mask. This could be achieved by developing a SIM reconstruction algorithm capable of accounting for the parasitic diffraction peaks, an approach that would require a detailed DMD forward model such as the one presented here. Implementing adaptive optics corrections could improve imaging quality and reduce artifacts, as has previously been reported (47, 56).

4: Conclusion

In this work, we constructed and validated a 3-color coherent DMD SIM instrument and developed a forward model for multicolor DMD diffraction. Using this analytical approach, we developed a forward model for DMD SIM patterns and new quantitative calibration tools including a method to directly map the microscope OTF. Using simulations, we showed that use of the real instrument OTF during SIM reconstruction provides a tangible benefit at low signal-to-noise ratios. We performed 2D linear SIM on a variety of samples, including the first demonstration of multicolor coherent 2D SIM imaging with a DMD, using a home built, hardware-triggered microscope. This work broadens potential applications of DMD SIM and opens new possibilities to create highly flexible multi-modal microscopes based around a DMD diffractive element.

Author contributions

Theoretical model, numerical simulations, hardware design and construction, software development, and instrument validation: PTB. Sample preparation and imaging: RK, GJS, PTB, DPS. Original concept, project management, and writing of manuscript: PTB, DPS.

Disclosures

The authors declare no conflicts of interest.

References

1. Shwetadwip Chowdhury, Will J Eldridge, Adam Wax, and Joseph A Izatt. Structured illumination microscopy for dual-modality 3D sub-diffraction resolution fluorescence and refractive-index reconstruction. *Biomedical Optics Express*, 8(12):5776–5793, December 2017. ISSN 2156-7085. doi: 10.1364/BOE.8.005776.

2. Seungwoo Shin, Doyeon Kim, Kyoohyun Kim, and Yongkeun Park. Super-resolution three-dimensional fluorescence and optical diffraction tomography of live cells using structured illumination generated by a digital micromirror device. *Scientific Reports*, 8(1):9183, June 2018. ISSN 2045-2322. doi: 10.1038/s41598-018-27399-w.

3. Furqan M Fazal and Steven M Block. Optical tweezers study life under tension. *Nature Photonics*, 5:318–321, May 2011. ISSN 1749-4885. doi: 10.1038/nphoton.2011.100.

4. Matthew J Comstock, Taekjip Ha, and Yann R Chemla. Ultrahigh-resolution optical trap with single-fluorophore sensitivity. *Nature Methods*, 8(4):335–340, April 2011. ISSN 1548-7091, 1548-7105. doi: 10.1038/nmeth.1574.

5. Cecilia Muldoon, Lukas Brandt, Jian Dong, Dustin Stuart, Edouard Brainis, Matthew Himsworth, and Axel Kuhn. Control and manipulation of cold atoms in optical tweezers. *New Journal of Physics*, 14(7):073051, jul 2012. doi: 10.1088/1367-2630/14/7/073051.

6. Martin J Booth. Adaptive optics in microscopy. *Philosophical Transactions of the Royal Society A: Mathematical, Physical and Engineering Sciences*, 365 (1861):2829–2843, sep 2007. doi: 10.1098/rsta.2007.0013.

7. Philip Zupancic, Philipp M. Preiss, Ruichao Ma, Alexander Lukin, M. Eric Tai, Matthew Rispoli, Rajibul Islam, and Markus Greiner. Ultra-precise holographic beam shaping for microscopic quantum control. *Optics Express*, 24(13):13881, jun 2016. doi: 10.1364/oe.24.013881.

8. George Patterson, Michael Davidson, Suliana Manley, and Jennifer Lippincott-Schwartz. Superresolution imaging using single-molecule localization. *Annual Review of Physical Chemistry*, 61:345–367, 2010. ISSN 0066-426X, 1545-1593. doi: 10.1146/annurev.physchem.012809.103444.

9. Jonatan Alvelid and Ilaria Testa. Fluorescence microscopy at the molecular scale. *Current Opinion in Biomedical Engineering*, 12:34–42, December 2019. ISSN 2468-4511. doi: 10.1016/j.cobme.2019.09.009.

10. T Dertinger, R Colyer, G Iyer, S Weiss, and J Enderlein. Fast, background-free, 3D super-resolution optical fluctuation imaging (SOFI). *Proceedings of the National Academy of Sciences of the United States of America*, 106(52):22287–22292, December 2009. ISSN 0027-8424, 1091-6490. doi: 10.1073/pnas.0907866106.

11. Siân Culley, Kalina L Tosheva, Pedro Matos Pereira, and Ricardo Henriques. SRRF: Universal live-cell super-resolution microscopy. *The International Journal of Biochemistry & Cell Biology*, 101:74–79, August 2018. ISSN 1357-2725, 1878-5875. doi: 10.1016/j.biocel.2018.05.014.

12. Stefan W. Hell and Jan Wichmann. Breaking the diffraction resolution limit by stimulated emission: stimulated-emission-depletion fluorescence microscopy. *Optics Letters*, 19(11):780, jun 1994. doi: 10.1364/ol.19.000780.

13. T. A. Klar, S. Jakobs, M. Dyba, A. Egner, and S. W. Hell. Fluorescence microscopy with diffraction resolution barrier broken by stimulated emission. *Proceedings of the National Academy of Sciences*, 97(15):8206–8210, jul 2000. doi: 10.1073/pnas.97.15.8206.

14. Klaus C. Gwosch, Jasmin K. Pape, Francisco Balzarotti, Philipp Hoess, Jan Ellenberg, Jonas Ries, and Stefan W. Hell. MINFLUX nanoscopy delivers 3d multicolor nanometer resolution in cells. *Nature Methods*, jan 2020. doi: 10.1038/s41592-019-0688-0.

15. M. Hofmann, C. Eggeling, S. Jakobs, and S. W. Hell. Breaking the diffraction barrier in fluorescence microscopy at low light intensities by using reversibly photoswitchable proteins. *Proceedings of the National Academy of Sciences*, 102(49):17565–17569, nov 2005. doi: 10.1073/pnas.0506010102.

16. Luciano A. Masullo, Andreas Bodén, Francesca Pennacchietti, Giovanna Coceano, Michael Ratz, and Ilaria Testa. Enhanced photon collection enables four dimensional fluorescence nanoscopy of living systems. *Nature Communications*, 9(1), aug 2018. doi: 10.1038/s41467-018-05799-w.

17. Rainer Heintzmann and Christoph G. Cremer. Laterally modulated excitation microscopy: improvement of resolution by using a diffraction grating. In Irving J. Bigio, Herbert Schneckenburger, Jan Slavik, Katarina Svanberg, and Pierre M. Viallet, editors, *Optical Biopsies and Microscopic Techniques III*. SPIE, jan 1999. doi: 10.1117/12.336833.

18. M. G. L. Gustafsson. Surpassing the lateral resolution limit by a factor of two using structured illumination microscopy. *Journal of Microscopy*, 198(2):82–87, may 2000. doi: 10.1046/j.1365-2818.2000.00710.x.

19. Brent Bailey, Daniel L. Farkas, D. Lansing Taylor, and Frederick Lanni. Enhancement of axial resolution in fluorescence microscopy by standing-wave excitation. *Nature*, 366(6450):44–48, nov 1993. doi: 10.1038/366044a0.

20. M. A. A. Neil, R. Juškaitis, and T. Wilson. Method of obtaining optical sectioning by using structured light in a conventional microscope. *Optics Letters*, 22 (24):1905, dec 1997. doi: 10.1364/ol.22.001905.

21. Mats G. L. Gustafsson, David A. Agard, and John W. Sedat. Doubling the lateral resolution of wide-field fluorescence microscopy using structured illumination. In Jose-Angel Conchello, Carol J. Cogswell, Andrew G. Tescher, and Tony Wilson, editors, *Three-Dimensional and Multidimensional Microscopy: Image Acquisition Processing VII*. SPIE, may 2000. doi: 10.1117/12.384189.

22. J. T. Frohn, H. F. Knapp, and A. Stemmer. True optical resolution beyond the Rayleigh limit achieved by standing wave illumination. *Proceedings of the National Academy of Sciences*, 97(13):7232–7236, jun 2000. doi: 10.1073/pnas.130181797.

23. J. T. Frohn, H. F. Knapp, and A. Stemmer. Three-dimensional resolution enhancement in fluorescence microscopy by harmonic excitation. *Optics Letters*, 26 (11):828, jun 2001. doi: 10.1364/ol.26.000828.

24. Mats G.L. Gustafsson, Lin Shao, Peter M. Carlton, C. J. Rachel Wang, Inna N. Golubovskaya, W. Zacheus Cande, David A. Agard, and John W. Sedat. Three-dimensional resolution doubling in wide-field fluorescence microscopy by structured illumination. *Biophysical Journal*, 94(12):4957–4970, jun 2008. doi: 10.1529/biophysj.107.120345.

25. L. Schermelleh, P. M. Carlton, S. Haase, L. Shao, L. Winoto, P. Kner, B. Burke, M. C. Cardoso, D. A. Agard, M. G. L. Gustafsson, H. Leonhardt, and J. W. Sedat. Subdiffraction multicolor imaging of the nuclear periphery with 3D structured illumination microscopy. *Science*, 320(5881):1332–1336, jun 2008. doi: 10.1126/science.1156947.

26. James D. Manton, Florian Ströhl, Reto Fiolka, Clemens F. Kaminski, and Eric J. Rees. Concepts for structured illumination microscopy with extended axial resolution through mirrored illumination. *Biomedical Optics Express*, 11(4):2098, mar 2020. doi: 10.1364/boe.382398.

27. Peter Kner, Bryant B Chhun, Eric R Griffis, Lukman Winoto, and Mats G L Gustafsson. Super-resolution video microscopy of live cells by structured illumination. *Nature Methods*, 6(5):339–342, apr 2009. doi: 10.1038/nmeth.1324.

28. Liisa M. Hirvonen, Kai Wicker, Ondrej Mandula, and Rainer Heintzmann. Structured illumination microscopy of a living cell. *European Biophysical Journal*, 38 (6):807–812, jun 2009. doi: 10.1007/s00249-009-0501-6.

29. Ronny Förster, Hui-Wen Lu-Walther, Aurélie Jost, Martin Kielhorn, Kai Wicker, and Rainer Heintzmann. Simple structured illumination microscope setup with high acquisition speed by using a spatial light modulator. *Optics Express*, 22(17):20663, aug 2014. doi: 10.1364/oe.22.020663.

30. Hui-Wen Lu-Walther, Martin Kielhorn, Ronny Förster, Aurélie Jost, Kai Wicker, and Rainer Heintzmann. fastSIM: a practical implementation of fast structured illumination microscopy. *Methods and Applications in Fluorescence*, 3(1):014001, jan 2015. doi: 10.1088/2050-6120/3/1/014001.

31. Michael Shaw, Lydia Zajiczek, and Kevin O'Holleran. High speed structured illumination microscopy in optically thick samples. *Methods*, 88:11–19, oct 2015. doi: 10.1016/j.ymeth.2015.03.020.

32. Andreas Markwirth, Mario Lachetta, Viola Mönkemöller, Rainer Heintzmann, Wolfgang Hübner, Thomas Huser, and Marcel Müller. Video-rate multi-color structured illumination microscopy with simultaneous real-time reconstruction. *Nature Communications*, 10(1), sep 2019. doi: 10.1038/s41467-019-12165-x.

33. Lin Shao, Peter Kner, E Hesper Rego, and Mats G L Gustafsson. Super-resolution 3D microscopy of live whole cells using structured illumination. *Nature Methods*, 8(12):1044–1046, oct 2011. doi: 10.1038/nmeth.1734.

34. R. Fiolka, L. Shao, E. H. Rego, M. W. Davidson, and M. G. L. Gustafsson. Time-lapse two-color 3D imaging of live cells with doubled resolution using structured illumination. *Proceedings of the National Academy of Sciences*, 109(14):5311–5315, mar 2012. doi: 10.1073/pnas.1119262109.

35. Loïc Reymond, Thomas Huser, Verena Ruprecht, and Stefan Wieser. Modulation-enhanced localization microscopy (meLM). *Journal of Physics: Photonics*, June 2020. ISSN 2515-7647. doi: 10.1088/2515-7647/ab9eac.

36. Laurence J. Young, Florian Ströhl, and Clemens F. Kaminski. A guide to structured illumination TIRF microscopy at high speed with multiple colors. *Journal of Visualized Experiments*, (111), may 2016. doi: 10.3791/53988.

37. Alice Sandmeyer, Mario Lachetta, Hauke Sandmeyer, Wolfgang Hübner, Thomas Huser, and Marcel Müller. DMD-based super-resolution structured illumination microscopy visualizes live cell dynamics at high speed and low cost. BioRxiv 10.1101/797670, 2019.

38. Ziwei Li, Qinrong Zhang, Shih-Wei Chou, Zachary Newman, Raphaël Turcotte, Ryan Natan, Qionghai Dai, Ehud Y. Isacoff, and Na Ji. Fast widefield imaging of neuronal structure and function with optical sectioning in vivo. *Science Advances*, 6(19):eaaz3870, may 2020. doi: 10.1126/sciadv.aaz3870.

39. Dan Dan, Ming Lei, Baoli Yao, Wen Wang, Martin Winterhalder, Andreas Zumbusch, Yujiao Qi, Liang Xia, Shaohui Yan, Yanlong Yang, Peng Gao, Tong Ye, and Wei Zhao. DMD-based LED-illumination super-resolution and optical sectioning microscopy. *Scientific Reports*, 3(1), jan 2013. doi: 10.1038/srep01116.

40. Loïc Reymond, Johannes Ziegler, Christian Knapp, Fung-Chen Wang, Thomas Huser, Verena Ruprecht, and Stefan Wieser. SIMPLE: Structured illumination based point localization estimator with enhanced precision. *Optics Express*, 27(17):24578, aug 2019. doi: 10.1364/oe.27.024578.

41. Kai Wicker and Rainer Heintzmann. Resolving a misconception about structured illumination. *Nature Photonics*, 8(5):342–344, apr 2014. doi: 10.1038/nphoton.2014.88.

42. Texas Instruments. Using lasers with DLP DMD technology. *TI DN*, 2509927, 2008.

43. Jinyang Liang. *High-Precision Laser Beam Shaping and Image Projection*. PhD thesis, The University of Texas at Austin, 2012.

44. R. Casini and P. G. Nelson. On the intensity distribution function of blazed reflective diffraction gratings. *Journal of the Optical Society of America A*, 31(10): 2179, sep 2014. doi: 10.1364/josaa.31.002179.

45. Neil W. Ashcroft and N. David Mermin. *Solid State Physics*, chapter 5. The Reciprocal Lattice, pages 85–94. Cengage Learning, Inc, 1976.

46. Bridget M. Hanser, Mats G. L. Gustafsson, David A. Agard, and John W. Sedat. Phase retrieval for high-numerical-aperture optical systems. *Optics Letters*, 28(10):801, may 2003. doi: 10.1364/ol.28.000801.

47. Mantas Žurauskas, Ian M. Dobbie, Richard M. Parton, Mick A. Phillips, Antonia Göhler, Ilan Davis, and Martin J. Booth. IsoSense: frequency enhanced sensorless adaptive optics through structured illumination. *Optica*, 6(3):370, mar 2019. doi: 10.1364/optica.6.000370.

48. A. Descloux, K. S. Grußmayer, and A. Radenovic. Parameter-free image resolution estimation based on decorrelation analysis. *Nature Methods*, 16(9): 918–924, aug 2019. doi: 10.1038/s41592-019-0515-7.

49. J Frank and M van Heel. Correspondence analysis of aligned images of biological particles. *Journal of Molecular Biology*, 161(1):134–137, October 1982. ISSN 0022-2836. doi: 10.1016/0022-2836(82)90282-0.

50. W O Saxton and W Baumeister. The correlation averaging of a regularly arranged bacterial cell envelope protein. *Journal of Microscopy*, 127(Pt 2):127–138, August 1982. ISSN 0022-2720. doi: 10.1111/j.1365-2818.1982.tb00405.x.

51. Robin Van den Eynde, Alice Sandmeyer, Wim Vandenberg, Sam Duwé, Wolfgang Hübner, Thomas Huser, Peter Dedecker, and Marcel Müller. Quantitative comparison of camera technologies for cost-effective super-resolution optical fluctuation imaging (sofi). *Journal of Physics: Photonics*, 1(4):044001, August 2019. ISSN 2515-7647. doi: 10.1088/2515-7647/ab36ae.

52. Andrew G York, Sapun H Parekh, Damian Dalle Nogare, Robert S Fischer, Kelsey Temprine, Marina Mione, Ajay B Chitnis, Christian A Combs, and Hari Shroff. Resolution doubling in live, multicellular organisms via multifocal structured illumination microscopy. *Nature Methods*, 9(7):749–754, may 2012. doi: 10.1038/nmeth.2025.

53. Knut Drescher, Jörn Dunkel, Luis H Cisneros, Sujoy Ganguly, and Raymond E Goldstein. Fluid dynamics and noise in bacterial cell-cell and cell-surface scattering. *Proceedings of the National Academy of Sciences of the United States of America*, 108(27):10940–10945, July 2011. ISSN 0027-8424, 1091-6490. doi: 10.1073/pnas.1019079108.

54. Jelmer Cnossen, Taylor Hinsdale, Rasmus Ø Thorsen, Marijn Siemons, Florian Schueder, Ralf Jungmann, Carlas S Smith, Bernd Rieger, and Sjoerd Stallinga. Localization microscopy at doubled precision with patterned illumination. *Nature methods*, 17(1):59–63, January 2020. ISSN 1548-7091, 1548-7105. doi: 10.1038/s41592-019-0657-7.

55. Liyan Song, Hui-Wen Lu-Walther, Ronny Förster, Aurélie Jost, Martin Kielhorn, Jianying Zhou, and Rainer Heintzmann. Fast structured illumination microscopy using rolling shutter cameras. *Measurement Science and Technology*, 27(5):055401, apr 2016. doi: 10.1088/0957-0233/27/5/055401.

56. Raphaël Turcotte, Yajie Liang, Masashi Tanimoto, Qinrong Zhang, Ziwei Li, Minoru Koyama, Eric Betzig, and Na Ji. Dynamic super-resolution structured illumination imaging in the living brain. *Proceedings of the National Academy of Sciences*, 116(19):9586–9591, apr 2019. doi: 10.1073/pnas.1819965116.